

Reinforced Imitative Trajectory Planning for Urban Automated Driving

Di Zeng¹, Ling Zheng^{1,2*}, Xiantong Yang¹, Yinong Li^{1,2}

¹College of Mechanical and Vehicle Engineering, Chongqing University, Shazheng Street, Chongqing, 40044, Chongqing, China.

^{2*}State Key Laboratory of Mechanical Transmission for Advanced Equipment, Chongqing University, Shazheng Street, Chongqing, 40044, Chongqing, China.

*Corresponding author(s). E-mail(s): zling@cqu.edu.cn;

Contributing authors: zigned@cqu.edu.cn; xiantongyang@cqu.edu.cn; ynli@cqu.edu.cn;

Abstract

Reinforcement learning (RL) faces challenges in trajectory planning for urban automated driving due to the poor convergence of RL and the difficulty in designing reward functions. The convergence problem is alleviated by combining RL with supervised learning. However, most existing approaches only reason one step ahead and lack the capability to plan for multiple future steps. Besides, although inverse reinforcement learning holds promise for solving the reward function design issue, existing methods for automated driving impose a linear structure assumption on reward functions, making them difficult to apply to urban automated driving. In light of these challenges, this paper proposes a novel RL-based trajectory planning method that integrates RL with imitation learning to enable multi-step planning. Furthermore, a transformer-based Bayesian reward function is developed, providing effective reward signals for RL in urban scenarios. Moreover, a hybrid-driven trajectory planning framework is proposed to enhance safety and interpretability. The proposed methods were validated on the large-scale real-world urban automated driving nuPlan dataset. The results demonstrated the significant superiority of the proposed methods over the baselines in terms of the closed-loop metrics. The code is available at https://github.com/Zigned/nuplan_zigned.

Keywords: Automated driving, Reinforcement learning, Trajectory planning, Closed-loop learning

1 Introduction

Urban automated driving (AD) presents significant challenges due to the complexity and diversity of traffic scenarios. To ease the difficulty, automated driving systems are usually divided into modules, such as perception, prediction, planning, and control. The planning module plays a crucial role in achieving a safe and comfortable driving experience since it determines the behavior of automated vehicles (AVs). Despite the

interpretability, conventional approaches for planning heavily rely on hand-crafted rules, making it difficult to handle complex and diverse situations. In contrast, learning-based approaches learn planning policies from large-scale data, thus circumventing the need for meticulously designed rules.

In recent years, imitation learning (IL) and reinforcement learning (RL) have dominated the

field of planning. IL learns the optimal planning policy from expert demonstrations. The most common category of IL is behavior cloning (BC), where expert demonstrations serve as supervisory signals to the agent. For example, the famous end-to-end framework proposed by NVIDIA maps raw camera inputs directly to steering commands [1]. In Ref. [2], sensor inputs of different modalities were utilized to enhance the urban driving ability of the BC-based planning model. More recently, the unified AD framework, named UniAD, incorporates perception and prediction tasks in one network to improve planning performance [3]. However, BC simply imitates the expert demonstrations in the collected states, resulting in poor generalization ability of the learned policy in new states, known as covariate shift [4]. To address this issue, DAgger employs the expert policy to take as input the visited state and output actions, which are aggregated into the training dataset [5]. However, DAgger and its extensions, such as SafeDAgger [6], require access to the expert policy during training, which is non-trivial.

RL is another promising solution for planning policy learning. In RL, the agent continuously interacts with the environment and optimizes its policy according to the rewards received from the environment. Unlike BC, RL trains the agent in a closed-loop manner, enabling the agent to continuously accumulate driving experience and understand the closed-loop effects of its actions [7].

RL has been successfully applied in highway driving tasks, such as lane keeping [8, 9], lane changing [10, 11], and traffic merging [12], where the agents are usually responsible for steering, throttle, and braking control according to vectorized traffic information (e.g., relative positions and relative velocities). RL has also been effectively implemented in urban scenarios. Urban scenarios involve more complex situations than highway scenarios, attributed to intricate road structures and diverse traffic participants with different behavioral patterns. Therefore, the state representation for urban scenarios is typically more complex, leading to an increase in both the parameter scale and structural complexity of neural networks used in RL. Consequently, the gradients computed by RL become insufficient to optimize such deep neural networks [13]. Tackling this issue, RL was combined with supervised learning. For instance, an IL agent was pre-trained to regularize the RL

agent training by imposing the Kullback-Leibler divergence between the two agents' policies in Ref. [14]. The RL agent determined a longitudinal target speed and a target lane according to bird's-eye-view (BEV) rasterized images, which incorporate map information and relative states between traffic participants. Roach [15] trains an RL agent with privileged BEV semantic segmentation images. Then, the RL agent is employed to collect a dataset, with which a downstream IL agent learns to control the steering, throttle, and braking.

However, most existing RL-based methods [16, 17, 13, 7] for AD only reason one step ahead and are not capable of planning for multiple future steps, which can be necessary to handle complex urban scenarios. Although an RL-based trajectory planning method, trajectory value learning (TRAVL), was proposed in Ref. [7], it has several drawbacks. First, TRAVL selects a trajectory from a finite trajectory set generated by predefined rules, which may reduce trajectory optimality. Second, generating the trajectory set and evaluating every trajectory online increase the computational complexity. Third, the applied scenarios of TRAVL were highway scenarios, while urban scenarios are much more complex.

Besides, most approaches rely on hand-crafted reward functions. Although inverse reinforcement learning (IRL) holds promise for solving the reward function design issue, existing methods [18, 19, 20] for AD mostly assume reward functions to be linear combinations of manually designed features, making them challenging to apply to urban traffic scenarios. Thus, designing effective reward functions for urban AD remains challenging.

Addressing the aforementioned limitations, this paper proposes a novel RL-based trajectory planning method, Reinforced Imitative Trajectory Planning (RITP), for urban automated driving. The contributions and novelty of this study are summarized as follows:

- 1) A novel RL-based trajectory planning method, RITP, is proposed. While most existing RL-based methods can only reason one step ahead, RITP integrates RL with IL, enabling planning for multiple future steps in complex urban scenarios. Unlike TRAVL, which plans trajectories with reduced optimality, RITP trains a transformer-based planner to explore the state

and trajectory spaces using trajectory noise and a transformer-based value function to evaluate the closed-loop effects of a plan. After training, the planner directly outputs a trajectory given a state, thus avoiding online trajectory generation and evaluation encountered by TRAVL.

- 2) A transformer-based Bayesian reward function is developed. The reward function is a Bayesian neural network without the linear structure assumption and models the uncertainty of the neural network, providing effective reward signals for reinforcement learning in urban scenarios.
- 3) A hybrid-driven trajectory planning framework is proposed to combine the advantages of data-driven and model-driven methods. The framework utilizes the trajectory planned by the RL agent to guide numerical optimization-based trajectory refinement, assessing the safety, legality, and comfort of the planned trajectories in an interpretable way.
- 4) The proposed methods were validated on the large-scale real-world urban automated driving nuPlan dataset [21, 22]. The effectiveness of the proposed methods was evaluated in both closed-loop non-reactive and closed-loop reactive experiments.

2 Reinforced Imitative Trajectory Planning

2.1 Preliminaries

AD can be modeled as a Markov decision process (MDP) defined by the tuple $(\mathcal{S}, \mathcal{A}, \mathcal{T}, R, \gamma)$, with states $s \in \mathcal{S}$, actions $a \in \mathcal{A}$, a transition function $\mathcal{T}(s_{t+1}|s_t, a_t) : \mathcal{S} \times \mathcal{S} \times \mathcal{A} \rightarrow [0, 1]$, a reward function $R(s) : \mathcal{S} \rightarrow \mathbb{R}$, and a discount factor $\gamma \in (0, 1]$. At each time step t , the ego agent (i.e., the AV) takes an action a_t given a state s_t according to its policy $\pi(s_t)$, receives a scalar reward r_{t+1} , and visits a new state s_{t+1} , resulting in an MDP sequence $(s_0, a_0, r_1, s_1, a_1, \dots, r_{T_m}, s_{T_m}, a_{T_m})$, where T_m is the time horizon. The return is defined as the discounted cumulative reward

$$G_t = \sum_{k=t+1}^{T_m} \gamma^{k-t-1} r_k$$

$$= \sum_{k=t+1}^{T_m} \gamma^{k-t-1} R(s_{k-1}, a_{k-1}). \quad (1)$$

In RL, the goal is to identify the optimal policy π_ϕ^* , parameterized by ϕ , that maximizes the expected return $\mathbb{E}_{s_k \sim p_{\pi_\phi}, a_k \sim \pi_\phi(s_k)} [G_0]$, where p_{π_ϕ} is the distribution of s_k under policy π_ϕ . In actor-critic methods, the optimal policy (i.e., the actor) can be obtained by maximizing an approximated value function (i.e., the critic). The value function is defined as $Q^\pi(s, a) = \mathbb{E}_{s_k \sim p_\pi, a_k \sim \pi(s_k)} [G_t | s_t = s, a_t = a]$, which can be learned with temporal difference learning based on the Bellman equation [23]

$$Q^\pi(s, a) = R(s, a) + \gamma \mathbb{E}_{s', a'} [Q^\pi(s', a')] \quad (2)$$

where (s', a') is the subsequent state-action pair of (s, a) .

For high-dimensional problems, such as AD, the value function is usually approximated by a neural network $Q_\theta(s, a)$ parameterized by θ . The deep Q-learning algorithm [24] optimizes the approximator $Q_\theta(s, a)$ to match a target q output by a secondary frozen target network $Q_{\theta'}(s, a)$

$$q = R(s, a) + \gamma Q_{\theta'}(s', a'), \quad (3)$$

where $a' \sim \pi_{\phi'}(s')$, $\pi_{\phi'}$ is a secondary frozen target actor network with parameter ϕ' . The parameters θ' and ϕ' are either periodically substituted by θ and ϕ or updated by a small proportion ξ at each time step, i.e., $\theta' \leftarrow \xi\theta + (1 - \xi)\theta'$ and $\phi' \leftarrow \xi\phi + (1 - \xi)\phi'$. However, the value estimated by $Q_\theta(s, a)$ is an overestimation [25]. Addressing this problem, the twin delayed deep deterministic policy gradient algorithm (TD3) [25] uses two critic networks $(Q_{\theta_1}, Q_{\theta_2})$ with two target critic networks $(Q_{\theta'_1}, Q_{\theta'_2})$ and replaces the target in Eq. (3) by

$$q = R(s, a) + \gamma \min_{i=1,2} Q_{\theta'_i}(s', \pi_\phi(s')). \quad (4)$$

To further reduce the estimation variance, TD3 adds a clipped normally distributed random noise ϵ to the target policy, resulting in a variant of Eq.

(4)

$$\begin{aligned}
q &= r + \gamma \min_{i=1,2} Q_{\theta'_i}(s', \pi_{\phi'}(s') + \epsilon), \\
\epsilon &\sim \text{clip}(\mathcal{N}(0, \sigma^2), -c, c),
\end{aligned} \tag{5}$$

where σ represents the standard deviation of the normal distribution and $[-c, c]$ defines the range of ϵ . Given the approximated value function and mini-batch size N , the policy is updated according to the deterministic policy gradient

$$N^{-1} \sum \nabla_a Q_{\theta_1}(s, a) \Big|_{a=\pi_\phi(s)} \nabla_\phi \pi_\phi(s) \tag{6}$$

every d iterations, known as the delayed policy updates.

2.2 Framework

As mentioned in Section 1, training a deep neural network-based policy for urban trajectory planning using conventional RL methods is intractable. Therefore, we integrate IL into RL with an actor-critic setting, proposing the reinforced imitative trajectory planning method, as shown in Fig. 1. Specifically, at each time step t , the actor takes an action a_t^0 given a state s_t . Concurrently, the action sampler generates S actions, i.e., $\{a_t^i\}_{i=1}^S$, for the same state s_t . The actions are defined as trajectories $\{a_t^i \mid a_t^i = \{\mathbf{p}_{t+j}^i\}_{j=1}^{T_p}\}_{i=0}^S$, with spatial location $\mathbf{p}_{t+j}^i = (x_{t+j}^i, y_{t+j}^i)$ and planning time horizon T_p . Afterward, only the action a_t^0 is sent to the environment, which then outputs the reward r_{t+1} and the subsequent state s_{t+1} . Next, observing the state s_{t+1} , the actor and action sampler output actions $\{a_{t+1}^i\}_{i=0}^S$, and the process repeats accordingly.

While the actor and the action sampler interact with the environment, the experience $(s_t, \{a_t^i\}_{i=0}^S, r_{t+1}, s_{t+1})$ is added to the replay buffer at each time step. Subsequently, a mini-batch of experiences is sampled from the replay buffer to update the critic network. Afterward, for each experience, the action with the highest value estimated by the critic network is selected from $\{a_t^i\}_{i=0}^S$ as the optimal action a_t^* . Finally, the optimal state-action pair (s_t, a_t^*) is used to update the actor via IL, and the updated actor is employed to interact with the environment at the next time step.

2.3 Environment

The environment can be built on a real-world urban automated driving dataset. During training, the environment is in non-reactive log-replay mode, where the other traffic participants, such as vehicles, pedestrians, and cyclists, do not react to the behavior of the ego agent and simply act according to the logged data. Upon receiving the action a_t^0 from the actor, the environment propagates the motion of the ego vehicle using an LQR-based trajectory tracker [26] and the kinematic bicycle model.

2.4 State Representation

The query-centric paradigm [27] is adopted to encode the traffic scene context. Consider a scenario with A agents (including the ego agent and the other traffic participants), M map polygons (either from the upstream perception module or the high-definition map), and T historical time steps. The i -th agent's information at historical time step $t-g$ ($g \in \{T-1, T-2, \dots, 0\}$) consists of the spatial position $\mathbf{p}_{t-g}^i = (x_{t-g}^i, y_{t-g}^i)$, the heading h_{t-g}^i , the temporal position $t-g$, the velocity $\mathbf{v}_{t-g}^i = (v_{t-g,x}^i, v_{t-g,y}^i)$, and the semantic attributes (e.g., agent type). Each map polygon (e.g., lanes, stop lines, and crosswalks) has P sample points with spatial positions $\mathbf{p}^i = (x^i, y^i)$, orientations h^i , and semantic attributes (e.g., traffic light status of a lane).

The query-centric paradigm builds an individual local spacetime coordinate system for the i -th agent at time step $t-g$ based on the position \mathbf{p}_{t-g}^i and the heading h_{t-g}^i or for the i -th map polygon based on the position and orientation of the first sample point of the polygon. Then, the information of an agent at time step $t-g$ is represented as $\mathbf{a}_{t-g}^i = (\|\mathbf{p}_{t-g}^i - \mathbf{p}_{t-g-1}^i\|_2, \langle \mathbf{h}_{t-g}^i, \mathbf{p}_{t-g}^i \rangle, \|\mathbf{v}_{t-g}^i\|_2, \langle \mathbf{h}_{t-g}^i, \mathbf{v}_{t-g}^i \rangle)$, where heading vector $\mathbf{h}_{t-g}^i = (\cos h_{t-g}^i, \sin h_{t-g}^i)$, and $\langle \cdot, \cdot \rangle$ denotes the angle between two vectors. The information of a sample point of a map polygon is represented as $\mathbf{m}^i = \|\mathbf{p}^i - \mathbf{p}^{i-1}\|_2$.

In order to incorporate the relative information between two spatial-temporal scene elements (e.g., an agent at some time step $t-g$ or a lane), a relative spatial-temporal positional encoding is employed. In particular, given a pair of spatial-temporal positions

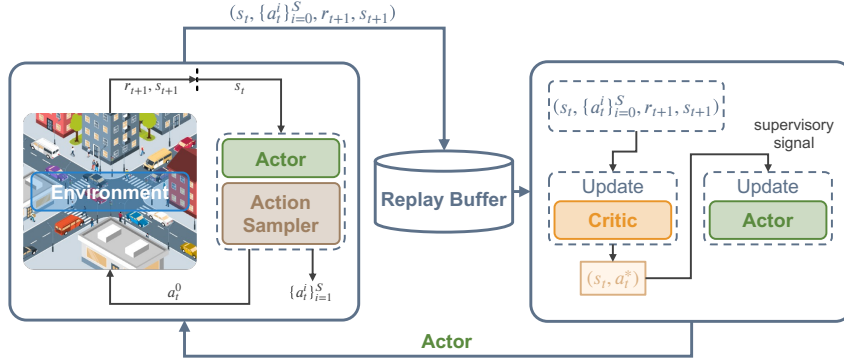


Fig. 1 Pipeline of the training process for the reinforced imitative trajectory planning

$(\mathbf{p}_{t-g}^i, h_{t-g}^i, t-g)$ and $(\mathbf{p}_{t-g'}^j, h_{t-g'}^j, t-g')$, the positional encoding is defined as $\mathbf{r}_{t-g' \rightarrow t-g}^{j \rightarrow i} = (\|\mathbf{p}_{t-g'}^j - \mathbf{p}_{t-g}^i\|_2, \text{atan2}(y_{t-g'}^j - y_{t-g}^i, x_{t-g'}^j - x_{t-g}^i) - h_{t-g}^i, h_{t-g'}^j - h_{t-g}^i, g-g')$. Additionally, the time gap $g-g'$ and the subscripts of the encodings for map polygons are omitted, i.e., $\mathbf{r}^{j \rightarrow i}$.

2.5 Actor Network: MotionFormer

Trajectory planning can be considered as a special case of trajectory prediction. Although trajectory prediction involves all agents while trajectory planning focuses solely on the ego agent, both tasks infer future trajectories based on traffic scene understanding. Therefore, a transformer-based actor network, referred to as MotionFormer, is constructed using QCNet architecture [27] for saving effort in actor network design, as shown in Fig. 2.

MotionFormer comprises an encoder that generates scene encodings and a decoder that decodes K future trajectories over a horizon of T_p time steps for each agent along with the estimated likelihoods utilizing the scene encodings. Each future trajectory is called a mode. During training, the trajectory with the highest likelihood is considered as the ego agent’s action. Additionally, the predicted trajectories for other agents are necessary for downstream post-optimization during testing, as explained in Section 4.

In the encoder, the Fourier embedding block first maps the state representation of the agents and map polygons, i.e., \mathbf{a}_{t-g}^i and \mathbf{m}^i , to the Fourier features [28] to enhance the learning of high-frequency signals. These Fourier features are then combined with the semantic attributes, such as the traffic light status of a map polygon and an

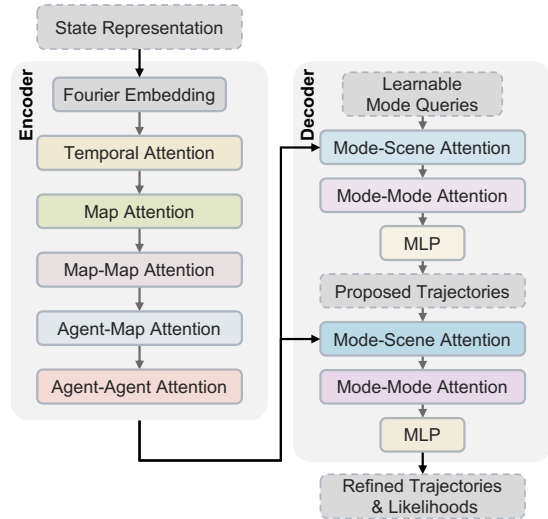


Fig. 2 Pipeline of MotionFormer

agent’s type, and processed through a multi-layer perceptron (MLP) to produce agent embeddings of shape $[A, T, D]$ and map embeddings of shape $[M, P, D]$. Here, P denotes the number of points per polygon, and D denotes the hidden feature dimension. Also, the relative positional encodings are mapped to Fourier features and passed through an MLP to generate relative positional embeddings.

To extract the temporal information of the agents, the temporal attention block performs self-attention across the agents’ historical time steps. Next, with the relative positional embeddings between the sample points of each polygon, the map attention block uses the map embedding for the first sample point to attend to those for the other sample points within the same polygon, reducing the map embeddings

from $[M, P, D]$ to $[M, D]$. Afterward, the map-map, agent-map, and agent-agent attention blocks perform self-attention across M polygons, cross-attention between agents and maps, and self-attention across A agents, respectively, to capture interactions between scene elements. The outputs of these three blocks are collectively referred to as scene encodings, i.e., map encodings of shape $[M, D]$ and agent encodings of shape $[A, T, D]$.

The decoder concatenated with the encoder first uses learnable mode queries to attend to the scene encodings, followed by the mode-mode self-attention and MLP processing, producing the proposed trajectories. Then, the proposed trajectories are processed through additional refinement blocks, including a mode-scene attention block, a mode-mode attention block, and MLPs to generate the refined trajectories and the corresponding likelihoods. Each mode-scene attention block includes cross-attention operations between modes and agent encodings and between modes and map encodings, thereby updating the mode queries with the scene encodings. Each mode-mode attention block employs self-attention across K modes to enhance the diversity of the modes.

In RL, exploration noise for actions is necessary. Standard RL algorithms add independently and identically distributed (i.i.d.) noise to each dimension of an action. However, the i.i.d. noise reduces the smoothness of the action defined as a trajectory, as depicted by the orange dashed line in Fig. 3. Therefore, we propose to add random trajectory noise to the refined trajectory with the highest estimated likelihood for the ego agent to facilitate exploration during training:

$$\begin{aligned}
 \tilde{a}_t &= \delta(a_t) \\
 &= \{(x_{t+j} + \alpha_j \epsilon \cos \theta_\epsilon, y_{t+j} + \alpha_j \epsilon \sin \theta_\epsilon)\}_{j=1}^{T_p} \\
 \epsilon &\sim \mathcal{N}(0, \beta \|\mathbf{p}_{t+T_p} - \mathbf{p}_t\|_2^2) \\
 \theta_\epsilon &\sim U[0, 2\pi) \\
 \alpha_j &= j/T_p,
 \end{aligned} \tag{7}$$

where constant $\beta > 0$ controls the strength of exploration, U denotes the uniform distribution, \mathbf{p}_t denotes the ego agent’s spatial position at time step t , and \mathbf{p}_{t+T_p} denotes the final spatial position of the action. Intuitively, the magnitude of the noise added to each position on the trajectory increases linearly over planning time step j until

it reaches a maximum value, which is determined by the exploration strength and displacement of the trajectory, as depicted by the green dash-dot line in Fig. 3.

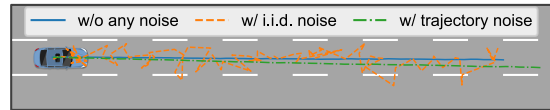


Fig. 3 Comparison between the trajectories without any noise, with i.i.d. noise, and with the proposed trajectory noise

2.6 Action Sampler

Ideally, the actor should imitate the optimal action a^* that maximizes the critic given a state s , i.e., $a^* = \arg \max_{a \in \mathcal{A}} Q(s, a)$. However, finding the optimal action is our goal in the first place. It is intractable because the action space \mathcal{A} for AD is continuous, high-dimensional, and with kinematic and dynamic constraints. Therefore, TRAVL [7] samples spline-based actions that are physically feasible for the ego agent in the Frenet frame of the road [29]. Inspired by TRAVL, we propose sampling actions based on piece-wise polynomials, allowing more flexible driving maneuvers.

Specifically, an action is decoupled into longitudinal and lateral trajectories

$$\begin{aligned}
 x_i(t) &= \mathbf{p}_{xi}^\top \cdot [1, t, t^2, t^3, t^4]^\top \\
 y_i(t) &= \mathbf{p}_{yi}^\top \cdot [1, t, t^2, t^3, t^4, t^5]^\top
 \end{aligned} \tag{8}$$

where $x_i(t)$ and $y_i(t)$ denote the i -th piece longitudinal and lateral trajectories in the Frenet frame, respectively and $\mathbf{p}_{xi} = (p_{xi,0}, p_{xi,1}, \dots, p_{xi,4})^\top$ and $\mathbf{p}_{yi} = (p_{yi,0}, p_{yi,1}, \dots, p_{yi,5})^\top$ are vectors of coefficients, such that each piece of a trajectory is smoothly connected with its predecessors and successors at the knots. By sampling knots with different lateral positions for lane-keeping and lane-changing maneuvers, a set of trajectories (i.e., action samples) is obtained, as shown in Fig. 4, where the lane-changing and lane-keeping trajectories consist of two pieces and three pieces, respectively. In practice, denser samples (up to 230,000 trajectories per state in our experiments) can be generated to minimize the risk of missing the optimal action by adjusting the time length of

each piece and varying the longitudinal and lateral positions of the knots, as shown in Fig. 5.

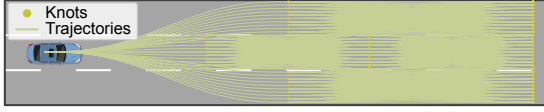


Fig. 4 Sampling actions based on piece-wise polynomials



Fig. 5 An example of action samples (only 1% of them are plotted for clarity) for a certain state

2.7 Critic Network: CriticFormer

In RL, the critic network evaluates how good an action is in a certain state. Aiming this, our critic network, namely CriticFormer, consists of a scene encoder, an action embedding block, and an action-scene attention block, as shown in Fig. 6. Essentially, CriticFormer embeds the action into a query to attend to traffic scene encodings and then generates the critic value. To be specific, considering the similarity of the actor and critic networks in traffic scene understanding, CriticFormer employs a scene encoder with the same architecture as the actor network’s encoder to encode the scene context. Furthermore, the action embedding block transforms the action into Fourier features. The Fourier features are further embedded by a GRU [30], the final hidden state of which serves as the action embedding.

In the action-scene attention block, the action embedding is successively updated by three cross-attention layers (action-history cross-attention, action-map cross-attention, and action-agent cross-attention) to attend to the ego agent’s encodings across T historical time steps, the map encodings, and the surrounding agents’ encodings at the current time step, respectively. For the ego agent at the current spatial-temporal position $(\mathbf{p}_t^{\text{ego}}, h_t^{\text{ego}}, t)$ and the i -th agent or i -th map polygon, the positional encodings for the three cross-attention layers are given by $\mathbf{r}_{t-g \rightarrow t}^{\text{ego} \rightarrow \text{ego}}$, $\mathbf{r}^{i \rightarrow \text{ego}}$, and $\mathbf{r}_{t \rightarrow t}^{i \rightarrow \text{ego}}$. Finally, the critic value is obtained by passing the updated query through an MLP.

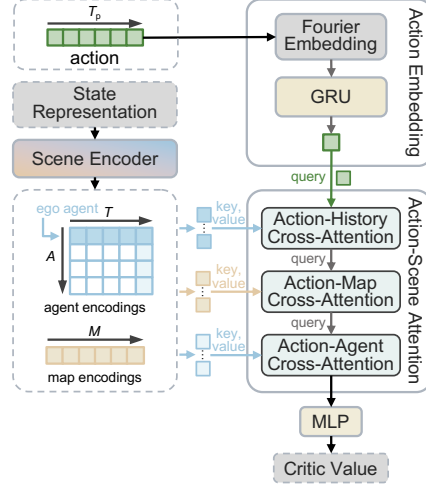


Fig. 6 Pipeline of CriticFormer

2.8 Training Objectives

Following QCNet [27], the ego agent’s action is parameterized as a mixture of Laplace distributions:

$$f\left(\{\mathbf{p}_{t+j}\}_{j=1}^{T_p}\right) = \sum_{k=1}^K \rho_k \prod_{j=1}^{T_p} \text{Laplace}\left(\mathbf{p}_{t+j} \mid \boldsymbol{\mu}_{t+j}^k, \boldsymbol{\sigma}_{t+j}^k\right) \quad (9)$$

with the mixing coefficient ρ_k , the location $\boldsymbol{\mu}_{t+j}^k$, and the scale $\boldsymbol{\sigma}_{t+j}^k$. MotionFormer is trained by imitation learning with a total loss defined as the sum of a classification loss \mathcal{L}_c , a regression loss for the proposed trajectory \mathcal{L}_p , and a regression loss for the refined trajectory \mathcal{L}_r :

$$\mathcal{L}_{\text{actor}} = \mathcal{L}_c + \mathcal{L}_p + \mathcal{L}_r, \quad (10)$$

where

$$\begin{aligned} \mathcal{L}_c &= -\log \sum_{k=1}^K \hat{\rho}_k \text{Laplace}\left(\mathbf{p}_{t+T_p}^{\text{target}} \mid \hat{\boldsymbol{\mu}}_{t+T_p}^k, \hat{\boldsymbol{\sigma}}_{t+T_p}^k\right) \\ \mathcal{L}_p &= -\frac{1}{T_p} \log \prod_{j=1}^{T_p} \text{Laplace}\left(\mathbf{p}_{t+j}^{\text{target}} \mid \check{\boldsymbol{\mu}}_{t+j}^*, \check{\boldsymbol{\sigma}}_{t+j}^*\right) \\ \mathcal{L}_r &= -\frac{1}{T_p} \log \prod_{j=1}^{T_p} \text{Laplace}\left(\mathbf{p}_{t+j}^{\text{target}} \mid \hat{\boldsymbol{\mu}}_{t+j}^*, \hat{\boldsymbol{\sigma}}_{t+j}^*\right), \end{aligned} \quad (11)$$

In Eq. (11), $\{\mathbf{p}_{t+j}^{\text{target}}\}_{j=1}^{T_p}$ denotes the supervisory signal, i.e., $a_t^* = \arg \max_{a \in \{a_t^i\}_{i=0}^S} Q(s_t, a)$. Remind that $\{a_t^i\}_{i=0}^S$ is the set of the ego agent's actions output by the actor and action sampler. $\hat{\boldsymbol{\mu}}_{t+j}^k$ and $\hat{\boldsymbol{\sigma}}_{t+j}^k$ are the j -th location and scale of the k -th refined trajectory, whose likelihood is $\hat{\rho}_k$. When computing the gradient of \mathcal{L}_c , the gradients of the locations and scales are omitted, and only the gradients of the mixing coefficients are retained. $\{\check{\boldsymbol{\mu}}_{t+j}^*\}_{j=1}^{T_p}$ and $\{\check{\boldsymbol{\sigma}}_{t+j}^*\}_{j=1}^{T_p}$ denote the locations and scales of the best-proposed trajectory among the K proposed trajectories in terms of the displacement error $\|\mathbf{p}_{t+T_p}^{\text{target}} - \check{\boldsymbol{\mu}}_{t+T_p}^k\|_2$. Similarly, $\{\hat{\boldsymbol{\mu}}_{t+j}^*\}_{j=1}^{T_p}$ and $\{\hat{\boldsymbol{\sigma}}_{t+j}^*\}_{j=1}^{T_p}$ denote the locations and scales of the best-refined trajectory. To facilitate stable training of the refinement blocks, the gradients of $\check{\boldsymbol{\mu}}_{t+j}^*$ and $\check{\boldsymbol{\sigma}}_{t+j}^*$ are omitted.

In practice, the MotionFormer is optimized to predict not only the ego agent's trajectory but also the trajectories of surrounding agents, whose supervisory signals are derived from the dataset. Because the predicted trajectories for surrounding agents are useful for the post-optimization (see Section 4).

For CriticFormer, the noise in Eq. (5) is replaced with the clipped version of the trajectory noise defined as Eq. (7), resulting in a target

$$q = r + \gamma \min_{i=1,2} Q_{\theta'_i}(s', \delta_c(\pi_{\phi'}(s'))) \quad (12)$$

Here, δ_c denote the same trajectory noise function as δ in Eq. (7) except for

$$\epsilon \sim \text{clip}(\mathcal{N}(0, \beta' \|\mathbf{p}_{t+T_p} - \mathbf{p}_t\|_2^2), -c \|\mathbf{p}_{t+T_p} - \mathbf{p}_t\|_2^2, c \|\mathbf{p}_{t+T_p} - \mathbf{p}_t\|_2^2) \quad (13)$$

where c is a constant that defines the boundaries of the clipping interval. In addition, d -delayed policy updates are employed to improve the quality of policy updates [25]. RITP algorithm is summarized in Algorithm 1.

3 Bayesian RewardFormer

The reward function is critical in RL. However, few studies concentrate on learning effective reward functions for urban AD. Besides, as introduced in Section 1, existing IRL methods for AD simplify the reward functions with the linear

Algorithm 1: Reinforced Imitative Trajectory Planning Algorithm

- 1 Initialize actor network π_ϕ and critic networks $Q_{\theta_1}, Q_{\theta_2}$ with parameters ϕ, θ_1, θ_2 ;
 - 2 Initialize target networks $\phi' \leftarrow \phi, \theta'_1 \leftarrow \theta_1, \theta'_2 \leftarrow \theta_2$;
 - 3 Initialize replay buffer \mathcal{B} ;
 - 4 Initialize $t = 0$;
 - 5 **while** $t < \text{maximum number of steps}$ **do**
 - 6 Select action with exploration noise in state s : $a^0 \leftarrow \delta(\pi_\phi(s))$, with δ defined by Eq. (7);
 - 7 Generate S action samples $\{a^i\}_{i=1}^S$ using the action sampler;
 - 8 Send a^0 to environment, receive reward r' and visit new state s' ;
 - 9 Store experience $(s, \{a^i\}_{i=0}^S, r', s')$ in \mathcal{B} ;
 - 10 Sample mini-batch of N experiences $(s, \{a^i\}_{i=0}^S, r', s')$ from \mathcal{B} ;
 - 11 Select action with clipped noise in sampled next state s' :
 $a' \leftarrow \delta_c(\pi_{\phi'}(s'))$, with δ_c defined by Eqs. (7) and (13);
 - 12 Compute target critic value: $q \leftarrow r + \gamma \min_{i=1,2} Q_{\theta'_i}(s', \delta_c(\pi_{\phi'}(s')))$;
 - 13 Update critic networks to minimize $\min_{\theta_i} N^{-1} \sum (q - Q_{\theta_i}(s, a))^2$;
 - 14 **if** $t \bmod d$ is 0 **then**
 - 15 Find optimal action in state s :
 $a^* = \arg \max_i Q_{\theta_1}(s, a^i)$;
 - 16 Update actor network with target a^* to minimize $N^{-1} \mathcal{L}_{\text{actor}}$ defined by Eqs. (10) and (11);
 - 17 Update target networks:
 $\theta'_i \leftarrow \xi \theta_i + (1 - \xi) \theta'_i$;
 $\phi'_i \leftarrow \xi \phi_i + (1 - \xi) \phi'_i$;
 - 18 $t \leftarrow t + 1$;
-

structure assumption, which limits the application of RL in urban AD. Addressing the reward function designing issue, we adapt our previous work, approximate variational reward learning (AVRL) [31], to urban AD. Due to space constraints, the following content will not cover the detailed derivation for AVRL.

3.1 Model Structure

AVRL models a reward function as a deep Bayesian neural network (BNN) [32], which estimates not only the reward for a state but also the uncertainty of the reward (i.e., how unconfident the model is). With variational inference [33], the deep BNN can be approximated by a deep neural network with dropout layers [34]. To encode the traffic scene context effectively, we also employ the query-centric state representation (see Section 2.4) and propose a transformer-based reward function, namely Bayesian RewardFormer.

Bayesian RewardFormer, as shown in Fig. 16, has the same architecture as the actor network’s encoder except for two modifications. First, the temporal attention block is removed because Bayesian RewardFormer takes as input agents’ current information \mathbf{a}_t^i and map information \mathbf{m}^i , omitting agents’ past information. Second, dropout layers are added after each fully connected layer in the attention blocks and the MLP to enable BNN approximation using dropout [35]. Specifically, let \mathbf{M}_i and \mathbf{b}_i be the weight

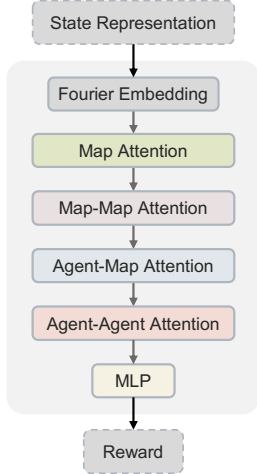


Fig. 7 Pipeline of Bayesian RewardFormer

matrix of dimensions $D_i \times D_{i-1}$ and the bias of dimensions D_i for the i -th fully connected layer of the attention blocks and MLP. After adding dropout layers, each weight matrix-dropout layer pair can be considered as a whole:

$$\mathbf{W}_i = \mathbf{M}_i \cdot \text{diag} \left([z_{i,j}]_{j=1}^{D_{i-1}} \right) \quad (14)$$

$$z_{i,j} \sim \text{Bernoulli} (p_i),$$

with dropout probabilities p_i for $i = 1, \dots, L$ and $j = 1, \dots, D_{i-1}$. L denotes the number of the fully connected layers of the attention blocks and MLP.

3.2 Training Objectives

Defining $\boldsymbol{\omega} = \{\mathbf{W}_i\}_{i=1}^L$ as the set of weight matrices for all L layers, the loss with respect to $\{\mathbf{M}_i\}_{i=1}^L$ and $\{\mathbf{b}_i\}_{i=1}^L$ for training Bayesian RewardFormer is

$$- \sum_{(s_t, a_t)} \log \frac{b^{R(\zeta|\hat{\boldsymbol{\omega}})}}{\sum_{\zeta'} b^{R(\zeta'|\hat{\boldsymbol{\omega}})}} + \sum_{i=1}^L \left(\frac{p_i}{2} \|\mathbf{M}_i\|_2^2 + \frac{1}{2} \|\mathbf{b}_i\|_2^2 \right), \quad (15)$$

with $\hat{\boldsymbol{\omega}}$ sampled from the distribution of $\boldsymbol{\omega}$. In Eq. (15), a_t denotes the ego agent’s action (trajectory) in state s_t in the dataset. $\zeta = \{\tilde{s}_{t+j}\}_{j=1}^{T_p}$ denotes the set of the predicted states that the ego agent will visit after taking action a_t , assuming that the ego agent follows the kinematic bicycle model and the other agents are in a non-reactive log-replay mode. ζ' represents the set of the predicted states for another possible action sampled based on polynomials in the Frenet frame of the road. $R(\zeta|\hat{\boldsymbol{\omega}})$ is defined as $\sum_{j=1}^{T_p} R(\tilde{s}_{t+j}|\hat{\boldsymbol{\omega}})$. The base b of the exponentiation is set to 1.1, which differs from the natural constant e employed in AVRL and improves the convergence when training the reward function.

3.3 Predicted Uncertainty-Penalized Reward

Neural networks make arbitrary predictions outside the domain they were trained on, known as epistemic uncertainty [36]. In the case of RL, a neural network-based reward function may output wrong rewards when the states differ from those in the dataset, thus leading to unexpected or even dangerous actions of the learned policy. Therefore, the reward at each RL time step is replaced with

the predicted uncertainty-penalized reward [31]:

$$\begin{aligned}
r_t &= \sum_{j=1}^{T_p} \tilde{r}_{t+j} - \lambda \tilde{u}_{t+j} \\
\tilde{r}_{t+j} &= \frac{1}{O} \sum_{o=1}^O R(\tilde{s}_{t+j} | \hat{\omega}_o) \\
\tilde{u}_{t+j} &= \tau^{-1} \sigma^2 + \frac{1}{O} \sum_{o=1}^O [R(\tilde{s}_{t+j} | \hat{\omega}_o)]^2 - \tilde{r}_{t+j}^2,
\end{aligned} \tag{16}$$

where \tilde{s}_{t+j} , \tilde{r}_{t+j} , and \tilde{u}_{t+j} denote the predicted state, reward mean, and reward uncertainty at future time step $t+j$. The uncertainty consists of the aleatoric uncertainty [36] ($\tau^{-1}\sigma^2$, with some model precision hyperparameter $\tau = 1$ and $\sigma = 1$) and the epistemic uncertainty (the reset terms except $\tau^{-1}\sigma^2$). The epistemic uncertainty is estimated by the variance of the O reward samples generated by O stochastic forward passes through Bayesian RewardFormer. Hyperparameter λ controls the strength of uncertainty-penalization. With the reward defined in Eq. (16), the ego agent is encouraged to minimize the epistemic uncertainty while maximizing the reward, which helps the learned policy to avoid unfamiliar situations [31].

4 Post-Optimizer

The epistemic uncertainty is inevitable for neural networks, including MotionFormer. MotionFormer may output dangerous actions in unfamiliar situations, e.g., a trajectory leading to a collision with a pedestrian. Therefore, a model-driven post-optimizer is developed to further optimize the action output by MotionFormer in the testing stage.

The post-optimizer consists of QP path planning and QP speed planning similar to Ref. [37], both of which are performed in the Frenet frame of the road. In the post-optimization, an action is decoupled into a path profile $y(x)$ and a speed profile $x(t)$, which are smoothing spline functions. Here, x , y , and t represent the longitudinal coordinate, lateral coordinate, and time, respectively.

Specifically, $y(x)$ is defined as

$$y(x) = \begin{cases} y_0(x - x_0) & x \in [x_0, x_1) \\ y_1(x - x_1) & x \in [x_1, x_2) \\ \dots & \dots \\ y_{n-1}(x - x_{n-1}) & x \in [x_{n-1}, x_n] \end{cases} \tag{17}$$

where $y_i(x) = p_{i,0} + p_{i,1}x + \dots + p_{i,m}x^m$, $i = 0, 1, \dots, n-1$, is a m -th degree polynomial function with the coefficient $\mathbf{p}_i = (p_{i,0}, p_{i,1}, \dots, p_{i,m})^\top$, and $\{x_0, x_1, \dots, x_n\}$ are the spline knots. The parameter vector of the smoothing spline function is denoted as $\mathbf{p} = (\mathbf{p}_0^\top, \mathbf{p}_1^\top, \dots, \mathbf{p}_{n-1}^\top)^\top$. $x(t)$ has the same form as $y(x)$.

The QP path planning is mathematically described as

$$\min_{\mathbf{p} \in \Omega} J(\mathbf{p}) = \sum_{i=0}^3 w_i J_i(\mathbf{p}) \tag{18}$$

subject to linear constraints $\mathbf{L}(\mathbf{p}) \leq \mathbf{0}$, where $\Omega = \{ \mathbf{p} : [x_0, x_n] \rightarrow \mathbb{R} \mid y, y^{(1)}, y^{(2)}, \dots, y^{(m)} \text{ is absolutely continuous and } \int_{x_0}^{x_n} (y^{(i)})^2 dx < \infty, i = 0, 1, \dots, m \}$, and w_i are weights. $y^{(i)}$ denotes the i -th derivative of y . In detail, the objective functionals are defined as

$$\begin{aligned}
J_0(\mathbf{p}) &= \int_{x_0}^{x_n} (y(x) - \hat{y}(x))^2 dx \\
J_1(\mathbf{p}) &= \int_{x_0}^{x_n} (y^{(1)}(x))^2 dx \\
J_2(\mathbf{p}) &= \int_{x_0}^{x_n} (y^{(2)}(x))^2 dx \\
J_3(\mathbf{p}) &= \int_{x_0}^{x_n} (y^{(3)}(x))^2 dx,
\end{aligned} \tag{19}$$

where $\hat{y}(x)$ represents the target path profile derived from the most likely trajectory output by MotionFormer. The linear constraints are related to collision avoidance, vehicle dynamics, and traffic regulations. For example, a constraint can be established based on the predicted trajectories of surrounding agents to avoid collisions.

Analogously, the QP speed planning is performed in the same manner as the QP path planning, except that the notation x is replaced by t , y is replaced by x , and J_1 , which encourages low speed, is removed. The post-optimized action is then obtained by combining the path and speed profiles. Essentially, solving the QP problems for path and speed planning involves finding a smooth trajectory that remains close to the original prediction while explicitly considering

collision avoidance, vehicle dynamics, traffic regulations, and other relevant factors. In addition, if the QP path or speed planning fails, the planned path profile will be the centerline of the lane, and the planned speed profile will be computed by an intelligent driver model (IDM [38]) with the same settings as Ref. [39].

5 Experiments

5.1 Experimental Settings

5.1.1 Dataset

We conducted experiments on the large-scale real-world automated driving nuPlan dataset [21, 22] to validate the effectiveness of our approach. The nuPlan dataset consists of 1282 hours of diverse urban driving scenarios from four cities (Las Vegas, Boston, Pittsburgh, and Singapore), including merges, lane changes, protected or unprotected turns, interactions with pedestrians and cyclists, and stop control in intersections. Each scenario lasts approximately 15 seconds and records the geometric and semantic information of surrounding map elements and traffic participants at a sampling rate of 10 Hz. Additionally, the motion states of traffic participants are recorded. The traffic light statuses are encoded into map elements. Our experiments randomly selected 10,000 scenarios comprising 70.1% training scenarios, 12.5% validation scenarios, and 17.4% testing scenarios.

5.1.2 Simulator and Metrics

Our experiments utilized the simulation and evaluation framework provided by the nuPlan dataset which enables closed-loop simulation considering the interactions between traffic participants. The simulator receives the planned trajectory of 8 seconds from the planner, uses an LQR as the tracker, and updates the motion state of the ego agent based on the kinematic bicycle model. In our experiments, the surrounding agents were successively in a closed-loop non-reactive log-replay mode and an IDM-based reactive mode. In the IDM-based reactive mode, the surrounding agents followed the paths in the dataset, while IDMs controlled the longitudinal motion.

To evaluate the performance of a planner, the closed-loop non-reactive score and the closed-loop

reactive score were adopted following the standard evaluation protocol of the nuPlan dataset. Each score is a weighted average of metrics, including no at-fault collisions, drivable area compliance, making progress, driving direction compliance, time-to-collision within bound, progress along route ratio, speed limit compliance, and comfort.

5.2 Baselines

Urban Driver [40] and QCNet [27] were adopted as the baselines in our experiments. The Urban Driver model embeds vectorized state representation of agents and map polygons into local features which are then passed through a global attention layer to predict trajectories. The Urban Driver model was trained using open-loop imitation learning implemented by nuPlan.

QCNet, which won the championship of the Argoverse 2 multi-agent motion forecasting competition, processes query-centric state representation into scene encodings using a factorized attention mechanism and predicts multimodal trajectories with DETR-like decoders [41]. We implemented QCNet in the nuPlan framework and trained it using open-loop imitation learning. Furthermore, the size of QCNet was reduced to enable training on a single NVIDIA RTX 4090 GPU with 24GB of VRAM, where the Urban Driver model and our MotionFormer, CriticFormer, and Bayesian RewardFormer were also trained. In order to compensate for the performance loss caused by model size reduction, a masked training strategy [42] and a self-distillation strategy [43, 44] were used for training QCNet, resulting in a variant of QCNet namely query-centric masked autoencoder (QCMAE).

5.3 Implementation details

We first trained Bayesian RewardFormer using AVRL. Then, QCMAE was trained using the masked training and self-distillation strategies. Next, with the trained QCMAE as a warm-start, MotionFormer was trained using the proposed RITP method. The optimizer, learning rate scheduler, and hyperparameters used for training are summarised in Table 1. For more details, please refer to the source code at https://github.com/Zigned/nuplan_zigned.

Table 1 Training configuration

Hyperparameters	AVRL	QCMAE	(H)RITP
Dropout probability p_i	0.1	0.1	0.1
Planning horizon T_p	80	80	80
Historical time horizon T	-	50	50
Hidden feature dimension D	64	64	64
Number of modes K	-	6	6
Exploration strength β	-	-	0.1
Policy noise strength β	-	-	0.2
Clipping boundary c	-	-	0.5
Optimizer	Adam [45]	AdamW [46]	AdamW
Learning rate	3e-7	5e-5→5e-4→5e-5	5e-5
Learning rate scheduler	-	OneCycle [47]	-
Batch size N	1	4	4, 1 ¹
Discount factor γ	-	-	0.99
Target update rate ξ	-	-	0.005
Update delay d	-	-	2
Uncertainty-penalization strength λ	-	-	1.5
Number of stochastic forward passes O	10	-	-
Max number of experiences in replay buffer	-	-	1e4
Total training epochs	10	60	-
Total training steps	-	-	1e5

¹ 4 for collecting experiences and 1 for optimization.

5.4 Comparison with Baselines

The results of the baselines and proposed approach on the testing set are summarized in Table 2. RITP involves training MotionFormer to predict the trajectories of all surrounding agents (referred to as multi-agent supervision hereafter), while RITP- focuses solely on optimizing the trajectory prediction for the ego agent. HRITP and HRITP-, where “H” stands for hybrid-driven, employ the post-optimizer to refine the output of MotionFormer.

Comparing the results of Urban Driver, QCMAE, and HRITP in Table 2, it can be concluded that our HRITP method substantially outperforms the baselines in terms of both the closed-loop non-reactive score (over 72% improvement) and the closed-loop reactive score (over 60% improvement). Furthermore, HRITP significantly reduces at-fault collisions and better controls vehicle spacing, improving the success rate by over 63% and 36% for the two modes, respectively. Fewer collisions happened in the closed-loop reactive mode than in the closed-loop non-reactive

mode because the surrounding agents in the latter mode automatically controlled the distance to the ego agent to avoid collisions.

The performance improvement of HRITP is attributed to several factors. Firstly, the superior performance of RITP over QCMAE demonstrates that RITP achieves better generalization through effective environment exploration based on the RL paradigm. Secondly, the comparison between RITP and HRITP highlights the effectiveness of the post-optimizer in refining MotionFormer’s output, thus preventing erroneous plans. Furthermore, the multi-agent supervision technique also contributes to performance improvement. This technique allows MotionFormer to fully utilize information from each scenario to model interactions between agents, thus improving the accuracy of trajectory prediction for the ego agent and surrounding agents. Note that predicted trajectories are crucial as they provide collision-avoidance constraints for the post-optimizer. We also found that integrating IL into RL is necessary. Without IL, MotionFormer trained solely by RL failed to generate a feasible trajectory and only produced a set of disorganized positions.

Table 2 Quantitative results on the testing set

Method	Closed-loop non-reactive				Closed-loop reactive			
	NAFC \uparrow	TTCWB \uparrow	SR \uparrow	Score \uparrow	NAFC \uparrow	TTCWB \uparrow	SR \uparrow	Score \uparrow
Urban Driver[40]	0.53	0.48	0.53	0.32	0.56	0.50	0.58	0.29
QCMAE	0.54	0.49	0.55	0.36	0.63	0.57	0.66	0.38
RITP-	0.75	0.69	0.76	0.39	0.81	0.78	0.82	0.41
HRITP-	0.86	0.78	0.87	0.55	0.86	0.76	0.88	0.54
RITP	0.80	0.74	0.81	0.51	0.82	0.78	0.83	0.52
HRITP	0.89	0.81	0.90	0.62	0.89	0.82	0.90	0.61

NAFC: no at-fault collisions. TTCWB: time-to-collision within bound. SR: success rate (the number of scenarios without at-fault collisions divided by the number of all scenarios). “ \uparrow ” denotes higher is better. The best result for each metric is in bold.

5.5 Qualitative Results

Some qualitative results on the testing set are presented in this section. Fig. 8 depicts a scenario of traversing an intersection, where the expert turned right with a trajectory represented by the orange curves in Fig. 8(a), (b), and (c). The ego vehicle controlled by UrbanDriver, QCMAE, and HRITP produced different trajectories of the ego vehicle as depicted by the blue curves in Fig. 8(a), (b), and (c). The top and bottom halves of Fig. 8(a), (b), and (c) represent the first and last frames of simulation, respectively. The motion states are shown in Fig. 8(d). As shown in Fig. 8, at the beginning of the simulation, UrbanDriver and QCMAE were able to drive within the lane. However, they drove out of the drivable area later, which was caused by covariate shift. In contrast, the ego vehicle controlled by HRITP entered the intersection following the preceding vehicle and properly stopped when the preceding vehicle stopped, probably due to pick-up or drop-off, just as the expert did.

Another scenario is shown in Fig. 9, where the ego vehicle was supposed to stop near the intersection. However, the UrbanDriver quickly veered off, running a red light and even driving into the wrong lane, as depicted in Fig. 9(a). QCMAE performed much better during the first 7 seconds but gradually drove out of the drivable area over the next 8 seconds, as presented in Fig. 9(b). By comparison, HRITP successfully guided the ego vehicle to slow down and keep a safe distance from the preceding vehicle, as shown in Fig. 9(c).

5.6 Discussion

The application of RL in trajectory planning for urban automated driving is limited by the poor convergence of RL and the difficulty of designing reward functions. The proposed RITP method integrates RL with IL to overcome the convergence problem. It trains CriticFormer to evaluate the closed-loop effect of an action, according to which supervisory signals are generated for IL. In contrast to RL, the gradients computed by IL are sufficient to optimize deep neural networks such as MotionFormer. Then, MotionFormer trained through IL explores the state and action spaces using the trajectory noise, thus resolving the suboptimality and the online computational complexity issues in TRAVL. Moreover, Bayesian RewardFormer provides effective reward signals for RL. As indicated by the results presented in the previous subsections, RITP significantly outperforms the baselines in terms of the closed-loop metrics. Another important reason for the effectiveness of RITP is that CriticFormer, MotionFormer, and Bayesian RewardFormer utilize the attention mechanism to extract information from the query-centric representation effectively. We also found that combining data-driven and model-driven methods can further improve the performance of RITP. Due to the inevitable epistemic uncertainty in neural networks, RITP might plan dangerous trajectories in unfamiliar situations. The post-optimizer refines the trajectories output by RITP to correct these wrong plans.

It is worth noting that common IL-based methods can be incorporated into the proposed RITP framework by simply replacing MotionFormer and

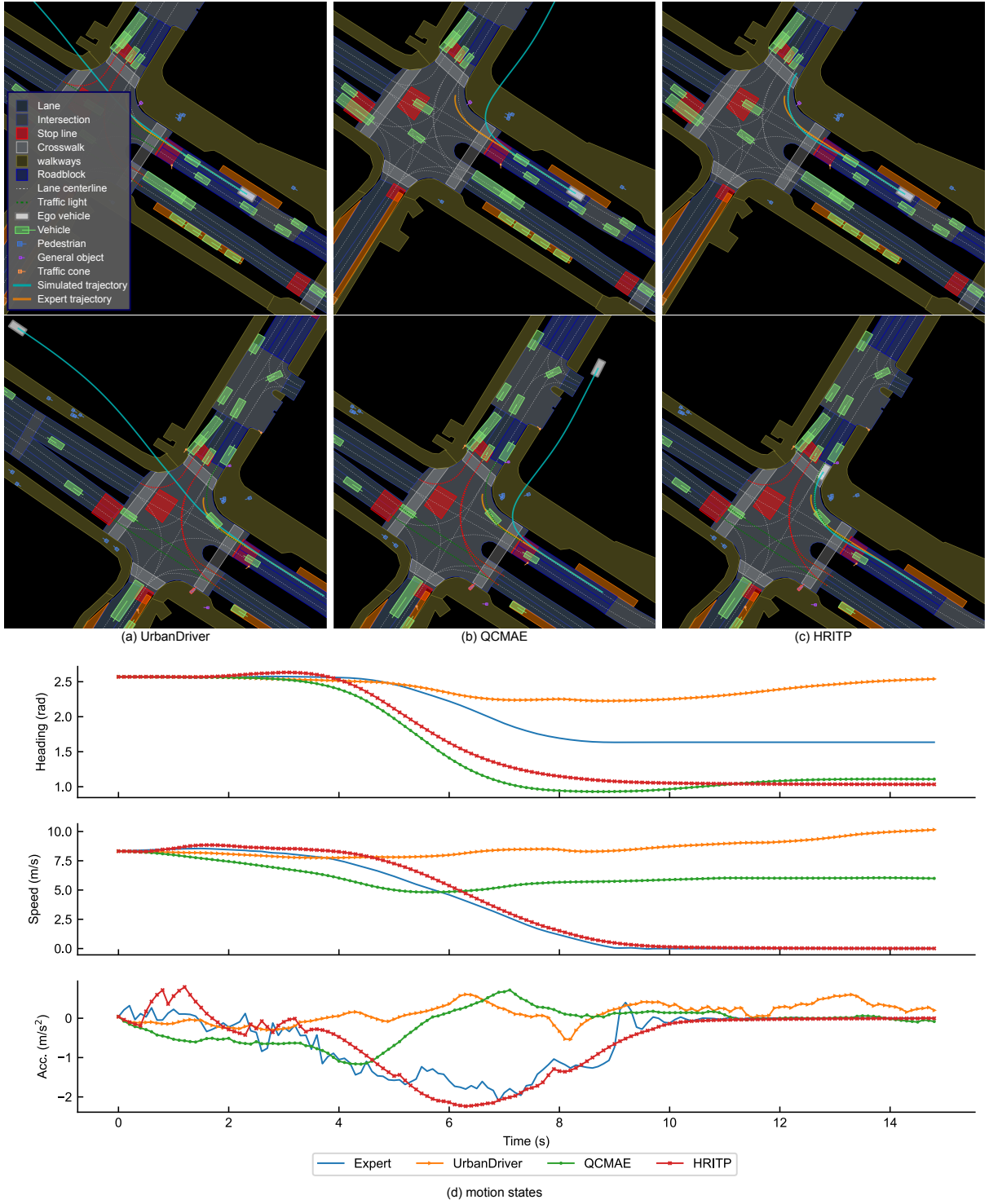


Fig. 8 A scenario of traversing an intersection

its training objective. For example, MotionFormer can be replaced by UniAD model [3], which takes

as input multi-view camera images, to enable end-to-end trajectory planning [13]. With RL,

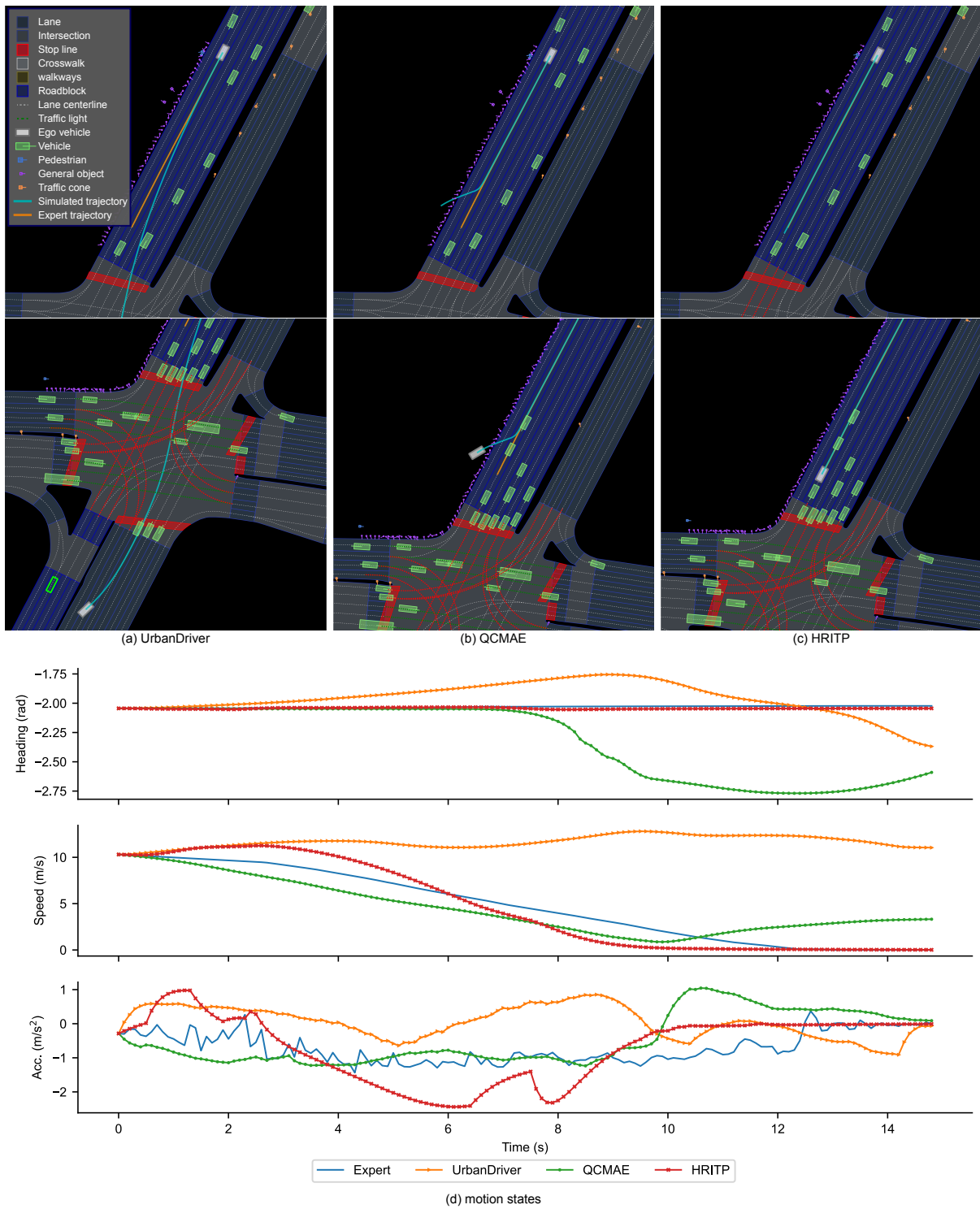


Fig. 9 A scenario of stopping near an intersection

the generalization ability of these models can be

enhanced to accomplish safe trajectory planning in urban scenarios.

However, we only use 10000 scenarios, a small portion of the full dataset, in our experiments due to hardware limitations. The performance of RITP using more scenarios is worth investigating.

6 Conclusion

This paper proposes a novel RL-based trajectory planning method for urban automated driving. The proposed method integrates IL into RL to improve the convergence, thus enabling planning for multiple future steps. Furthermore, a transformer-based Bayesian reward function is developed, which removes the linear structure assumption imposed by most existing methods and is applicable to RL in urban scenarios. Besides, a hybrid-driven trajectory planning framework is proposed to enhance the feasibility of the trajectories planned by the RL agent. The results of the experiments conducted on the large-scale real-world urban automated driving nuPlan dataset indicate that the proposed methods significantly outperform baselines in terms of the closed-loop metrics.

Nomenclature

AD	Automated driving
AV(s)	Automated vehicle(s)
BC	Behavior cloning
BEV	Bird’s-eye-view
HRITP	Hybrid-driven reinforced imitative trajectory planning
IL	Imitation learning
IRL	Inverse reinforcement learning
LQR	Linear quadratic regulator
MDP	Markov decision process
MLP(s)	Multi-layer perceptron(s)
QCMAC	Query-centric masked autoencoder
RITP	Reinforced imitative trajectory planning
RL	Reinforcement learning
TRAVL	Trajectory value learning

Acknowledgements. This work was supported by the National Natural Science Foundation of China (Grant No. 52472424) and the Fundamental Research Funds for the Central Universities (2023CDJXY-021).

Declarations

Conflict of interest On behalf of all authors, the corresponding author states that there is no conflict of interest.

References

- [1] M. Bojarski, D. Del Testa, D. Dworakowski, B. Firner, B. Flepp, P. Goyal, L. D. Jackel, M. Monfort, U. Muller, J. Zhang, et al., End to end learning for self-driving cars, arXiv preprint arXiv:1604.07316 (2016).
- [2] D. Chen, P. Krähenbühl, Learning from all vehicles, in: Proceedings of the IEEE/CVF Conference on Computer Vision and Pattern Recognition (CVPR), 2022, pp. 17222–17231.
- [3] Y. Hu, J. Yang, L. Chen, K. Li, C. Sima, X. Zhu, S. Chai, S. Du, T. Lin, W. Wang, L. Lu, X. Jia, Q. Liu, J. Dai, Y. Qiao, H. Li, Planning-oriented autonomous driving, in: Proceedings of the IEEE/CVF Conference on Computer Vision and Pattern Recognition (CVPR), 2023, pp. 17853–17862.
- [4] S. Ross, D. Bagnell, Efficient reductions for imitation learning, in: Y. W. Teh, M. Titterton (Eds.), Proceedings of the Thirteenth International Conference on Artificial Intelligence and Statistics, volume 9 of *Proceedings of Machine Learning Research*, PMLR, Chia Laguna Resort, Sardinia, Italy, 2010, pp. 661–668.
- [5] S. Ross, G. Gordon, D. Bagnell, A reduction of imitation learning and structured prediction to no-regret online learning, in: G. Gordon, D. Dunson, M. Dudík (Eds.), Proceedings of the Fourteenth International Conference on Artificial Intelligence and Statistics, volume 15 of *Proceedings of Machine Learning Research*, PMLR, Fort Lauderdale, FL, USA, 2011, pp. 627–635.
- [6] J. Zhang, K. Cho, Query-efficient imitation learning for end-to-end simulated driving, Proceedings of the AAAI Conference on Artificial Intelligence 31 (2017). doi:[10.1609/aaai.v31i1.10857](https://doi.org/10.1609/aaai.v31i1.10857).
- [7] C. Zhang, R. Guo, W. Zeng, Y. Xiong, B. Dai, R. Hu, M. Ren, R. Urtasun, Rethinking closed-loop training for autonomous driving, in: S. Avidan, G. Brostow, M. Cissé,

- G. M. Farinella, T. Hassner (Eds.), *Computer Vision – ECCV 2022*, Springer Nature Switzerland, Cham, 2022, pp. 264–282.
- [8] A. E. Sallab, M. Abdou, E. Perot, S. Yogamani, End-to-end deep reinforcement learning for lane keeping assist, *arXiv preprint arXiv:1612.04340* (2016).
- [9] A. Kendall, J. Hawke, D. Janz, P. Mazur, D. Reda, J.-M. Allen, V.-D. Lam, A. Bewley, A. Shah, Learning to drive in a day, in: *2019 International Conference on Robotics and Automation (ICRA)*, 2019, pp. 8248–8254. doi:[10.1109/ICRA.2019.8793742](https://doi.org/10.1109/ICRA.2019.8793742).
- [10] G. Li, Y. Qiu, Y. Yang, Z. Li, S. Li, W. Chu, P. Green, S. E. Li, Lane change strategies for autonomous vehicles: A deep reinforcement learning approach based on transformer, *IEEE Transactions on Intelligent Vehicles* 8 (2023) 2197–2211. doi:[10.1109/TIV.2022.3227921](https://doi.org/10.1109/TIV.2022.3227921).
- [11] G. Wang, J. Hu, Z. Li, L. Li, Harmonious lane changing via deep reinforcement learning, *IEEE Transactions on Intelligent Transportation Systems* 23 (2022) 4642–4650. doi:[10.1109/TITS.2020.3047129](https://doi.org/10.1109/TITS.2020.3047129).
- [12] P. Wang, C.-Y. Chan, Formulation of deep reinforcement learning architecture toward autonomous driving for on-ramp merge, in: *2017 IEEE 20th International Conference on Intelligent Transportation Systems (ITSC)*, 2017, pp. 1–6. doi:[10.1109/ITSC.2017.8317735](https://doi.org/10.1109/ITSC.2017.8317735).
- [13] L. Chen, P. Wu, K. Chitta, B. Jaeger, A. Geiger, H. Li, End-to-end autonomous driving: Challenges and frontiers, *arXiv preprint arXiv:2306.16927* (2023).
- [14] Z. Huang, J. Wu, C. Lv, Efficient deep reinforcement learning with imitative expert priors for autonomous driving, *IEEE Transactions on Neural Networks and Learning Systems* 34 (2023) 7391–7403. doi:[10.1109/TNNLS.2022.3142822](https://doi.org/10.1109/TNNLS.2022.3142822).
- [15] Z. Zhang, A. Liniger, D. Dai, F. Yu, L. Van Gool, End-to-end urban driving by imitating a reinforcement learning coach, in: *Proceedings of the IEEE/CVF International Conference on Computer Vision (ICCV)*, 2021, pp. 15222–15232.
- [16] Z. Zhu, H. Zhao, A survey of deep rl and il for autonomous driving policy learning, *IEEE Transactions on Intelligent Transportation Systems* 23 (2022) 14043–14065. doi:[10.1109/TITS.2021.3134702](https://doi.org/10.1109/TITS.2021.3134702).
- [17] B. R. Kiran, I. Sobh, V. Talpaert, P. Mannion, A. A. A. Sallab, S. Yogamani, P. Pérez, Deep reinforcement learning for autonomous driving: A survey, *IEEE Transactions on Intelligent Transportation Systems* 23 (2022) 4909–4926. doi:[10.1109/TITS.2021.3054625](https://doi.org/10.1109/TITS.2021.3054625).
- [18] S. Sharifzadeh, I. Chiotellis, R. Triebel, D. Cremers, Learning to drive using inverse reinforcement learning and deep q-networks, *arXiv preprint arXiv:1612.03653* (2016).
- [19] Z. Wu, L. Sun, W. Zhan, C. Yang, M. Tomizuka, Efficient sampling-based maximum entropy inverse reinforcement learning with application to autonomous driving, *IEEE Robotics and Automation Letters* 5 (2020) 5355–5362. doi:[10.1109/LRA.2020.3005126](https://doi.org/10.1109/LRA.2020.3005126).
- [20] Z. Huang, J. Wu, C. Lv, Driving behavior modeling using naturalistic human driving data with inverse reinforcement learning, *IEEE Transactions on Intelligent Transportation Systems* 23 (2022) 10239–10251. doi:[10.1109/TITS.2021.3088935](https://doi.org/10.1109/TITS.2021.3088935).
- [21] H. Caesar, J. Kabzan, K. S. Tan, W. K. Fong, E. Wolff, A. Lang, L. Fletcher, O. Beijbom, S. Omari, nuplan: A closed-loop ml-based planning benchmark for autonomous vehicles, *arXiv preprint arXiv:2106.11810* (2021).
- [22] N. Karnchanachari, D. Geromichalos, K. S. Tan, N. Li, C. Eriksen, S. Yaghoubi, N. Mehdipour, G. Bernasconi, W. K. Fong, Y. Guo, et al., Towards learning-based planning: The nuplan benchmark for real-world autonomous driving, *arXiv preprint arXiv:2403.04133* (2024).
- [23] R. S. Sutton, Learning to predict by the methods of temporal differences, *Machine learning* 3 (1988) 9–44.
- [24] V. Mnih, K. Kavukcuoglu, D. Silver, A. A. Rusu, J. Veness, M. G. Bellemare, A. Graves, M. Riedmiller, A. K. Fidjeland, G. Ostrovski, et al., Human-level control through deep reinforcement learning, *nature* 518 (2015) 529–533. doi:[10.1038/nature14236](https://doi.org/10.1038/nature14236).

- [25] S. Fujimoto, H. van Hoof, D. Meger, Addressing function approximation error in actor-critic methods, in: J. Dy, A. Krause (Eds.), Proceedings of the 35th International Conference on Machine Learning, volume 80 of *Proceedings of Machine Learning Research*, PMLR, 2018, pp. 1587–1596.
- [26] J. Liu, Z. Yang, Z. Huang, W. Li, S. Dang, H. Li, Simulation performance evaluation of pure pursuit, stanley, lqr, mpc controller for autonomous vehicles, in: 2021 IEEE International Conference on Real-time Computing and Robotics (RCAR), 2021, pp. 1444–1449.
- [27] Z. Zhou, J. Wang, Y.-H. Li, Y.-K. Huang, Query-centric trajectory prediction, in: Proceedings of the IEEE/CVF Conference on Computer Vision and Pattern Recognition (CVPR), 2023, pp. 17863–17873.
- [28] M. Tancik, P. Srinivasan, B. Mildenhall, S. Fridovich-Keil, N. Raghavan, U. Singhal, R. Ramamoorthi, J. Barron, R. Ng, Fourier features let networks learn high frequency functions in low dimensional domains, in: H. Larochelle, M. Ranzato, R. Hadsell, M. Balcan, H. Lin (Eds.), Advances in Neural Information Processing Systems, volume 33, Curran Associates, Inc., 2020, pp. 7537–7547.
- [29] M. Werling, J. Ziegler, S. Kammel, S. Thrun, Optimal trajectory generation for dynamic street scenarios in a frenét frame, in: 2010 IEEE International Conference on Robotics and Automation, 2010, pp. 987–993. doi:[10.1109/ROBOT.2010.5509799](https://doi.org/10.1109/ROBOT.2010.5509799).
- [30] K. Cho, B. van Merriënboer, C. Gulcehre, D. Bahdanau, F. Bougares, H. Schwenk, Y. Bengio, Learning phrase representations using RNN encoder–decoder for statistical machine translation, in: A. Moschitti, B. Pang, W. Daelemans (Eds.), Proceedings of the 2014 Conference on Empirical Methods in Natural Language Processing (EMNLP), Association for Computational Linguistics, Doha, Qatar, 2014, pp. 1724–1734. doi:[10.3115/v1/D14-1179](https://doi.org/10.3115/v1/D14-1179).
- [31] D. Zeng, L. Zheng, X. Yang, Y. Li, Uncertainty-aware human-like driving policy learning with deep bayesian inverse reinforcement learning, *Transportmetrica A: Transport Science* 0 (2024) 1–25. doi:[10.1080/23249935.2024.2318621](https://doi.org/10.1080/23249935.2024.2318621).
- [32] R. M. Neal, Bayesian Learning for Neural Networks, volume 118, Springer, New York, NY, 2012.
- [33] D. M. Blei, A. Kucukelbir, J. D. McAuliffe, Variational inference: A review for statisticians, *Journal of the American Statistical Association* 112 (2017) 859–877.
- [34] G. E. Hinton, N. Srivastava, A. Krizhevsky, I. Sutskever, R. R. Salakhutdinov, Improving neural networks by preventing co-adaptation of feature detectors, arXiv preprint arXiv:1207.0580 (2012).
- [35] Y. Gal, Z. Ghahramani, Dropout as a bayesian approximation: Representing model uncertainty in deep learning, in: International Conference on Machine Learning, PMLR, 2016, pp. 1050–1059.
- [36] Y. Gal, Uncertainty in deep learning (2016).
- [37] H. Fan, F. Zhu, C. Liu, L. Zhang, L. Zhuang, D. Li, W. Zhu, J. Hu, H. Li, Q. Kong, Baidu apollo em motion planner, arXiv preprint arXiv:1807.08048 (2018).
- [38] M. Treiber, A. Hennecke, D. Helbing, Congested traffic states in empirical observations and microscopic simulations, *Phys. Rev. E* 62 (2000) 1805–1824. doi:[10.1103/PhysRevE.62.1805](https://doi.org/10.1103/PhysRevE.62.1805).
- [39] D. Dauner, M. Hallgarten, A. Geiger, K. Chitta, Parting with misconceptions about learning-based vehicle motion planning, in: J. Tan, M. Toussaint, K. Darvish (Eds.), Proceedings of The 7th Conference on Robot Learning, volume 229 of *Proceedings of Machine Learning Research*, PMLR, 2023, pp. 1268–1281.
- [40] O. Scheel, L. Bergamini, M. Wolczyk, B. Osiński, P. Ondruska, Urban driver: Learning to drive from real-world demonstrations using policy gradients, in: A. Faust, D. Hsu, G. Neumann (Eds.), Proceedings of the 5th Conference on Robot Learning, volume 164 of *Proceedings of Machine Learning Research*, PMLR, 2022, pp. 718–728.
- [41] N. Carion, F. Massa, G. Synnaeve, N. Usunier, A. Kirillov, S. Zagoruyko, End-to-end object detection with transformers, in: A. Vedaldi, H. Bischof, T. Brox, J.-M. Frahm (Eds.), Computer Vision – ECCV 2020, Springer International Publishing, Cham, 2020, pp. 213–229.

- [42] Z. Lan, Y. Jiang, Y. Mu, C. Chen, S. E. Li, SEPT: Towards efficient scene representation learning for motion prediction, in: The Twelfth International Conference on Learning Representations, 2024.
- [43] G. Chen, W. Choi, X. Yu, T. Han, M. Chandraker, Learning efficient object detection models with knowledge distillation, in: I. Guyon, U. V. Luxburg, S. Bengio, H. Wallach, R. Fergus, S. Vishwanathan, R. Garnett (Eds.), Advances in Neural Information Processing Systems, volume 30, Curran Associates, Inc., 2017.
- [44] Y. Shen, L. Xu, Y. Yang, Y. Li, Y. Guo, Self-distillation from the last mini-batch for consistency regularization, in: Proceedings of the IEEE/CVF Conference on Computer Vision and Pattern Recognition (CVPR), 2022, pp. 11943–11952.
- [45] D. P. Kingma, J. Ba, Adam: A method for stochastic optimization, arXiv preprint arXiv:1412.6980 (2014).
- [46] I. Loshchilov, F. Hutter, Decoupled weight decay regularization, arXiv preprint arXiv:1711.05101 (2017).
- [47] L. N. Smith, N. Topin, Super-convergence: very fast training of neural networks using large learning rates, in: T. Pham (Ed.), Artificial Intelligence and Machine Learning for Multi-Domain Operations Applications, volume 11006, International Society for Optics and Photonics, SPIE, 2019, p. 1100612. doi:[10.1117/12.2520589](https://doi.org/10.1117/12.2520589).